Nanoparticle Cluster Arrays for High-Performance SERS through Directed Self-Assembly on Flat Substrates and on Optical Fibers

Fung Ling Yap,[†] Praveen Thoniyot,[‡,*] Sathiyamoorthy Krishnan,[§] and Sivashankar Krishnamoorthy[†,*]

[†]Institute of Materials Research and Engineering (IMRE), Agency for Science, Technology and Research (A*STAR), 3, Research Link, 117602, Singapore, [§]School of Mechanical and Aerospace Engineering, Nanyang Technology University (NTU), 639815, Singapore, and [‡]Singapore Bioimaging Consortium (SBIC), Agency for Science, Technology and Research (A*STAR), 11 Biopolis Way, Helios, #02-02, 138667 Singapore

ABSTRACT We demonstrate template-guided self-assembly of gold nanoparticles into ordered arrays of uniform clusters suitable for high-performance SERS on both flat (silicon or glass) chips and an optical fiber faucet. Cluster formation is driven by electrostatic self-assembly of anionic citrate-stabilized gold nanoparticles (~11.6 nm diameter) onto two-dimensionally ordered polyelectrolyte templates realized by self-assembly of polystyrene-block-poly(2-vinylpyridine). A systematic variation is demonstrated for the number of particles ($N \approx 5$, 8, 13, or 18) per cluster as well as intercluster separations ($S_c \approx 37-10$ nm). Minimum interparticle separations of <5 nm, intercluster separations of ~10 nm, and nanoparticle densities on surfaces as high as $\sim 7 \times 10^{11}$/in.^{2} are demonstrated. Geometric modeling is used to support experimental data toward estimation of interparticle and intercluster separations in cluster arrays. Optical modeling and simulations using the finite difference time domain method are used to establish the influence of cluster size, shape, and intercluster separations on the optical properties of the cluster arrays in relation to their SERS performance. Excellent SERS performance, as evidenced by a high enhancement factor, $>10^8$ on flat chips and $>10^7$ for remote sensing, using SERS-enabled optical fibers is demonstrated. The best performing cluster arrays in both cases are achievable without the use of any expensive equipment or clean room processing. The demonstrated approach paves the way to significantly low-cost and high-throughput production of sensor chips or 3D-configured surfaces for remote sensing applications.

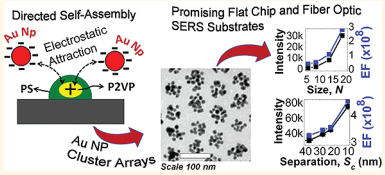

KEYWORDS: self-assembly · nanoparticle clusters · SERS · block copolymer · LSPR · plasmonic coupling · remote-sensing

Advancements in technologies for applications such as life care, environmental monitoring, food safety, and defense present ever-increasing needs for high-performance analytical tools that are simple to make, low-cost, and easy to integrate. Surface enhanced Raman spectroscopy (SERS) is a highly promising tool in this direction due to its ability for label-free analysis with high sensitivity, surface selectivity, and multiplexing capabilities. SERS has recently proved to be promising toward sensing of diverse analytes, *e.g.*, metabolites, disease markers, pathogens, terrorism markers, hazardous pollutants, and illegal drugs for exploitation in biomedicine, food quality control, environmental monitoring, and security applications.[1−5] How the SERS substrate is fabricated and how well it performs in delivering high sensitivity, low signal variability, high chemical/mechanical stability, low-cost fabrication, and ease of translation onto 3D optical constructs play a determining role in enabling other capabilities that govern the final success of the SERS sensor. To achieve this end, low-cost fabrication of SERS substrates consisting of metal nanostructures with well-defined geometries and predictable optical response and that can further be tailored to yield high SERS enhancements is being heavily researched. While numerous SERS substrates have been described in the literature, there is often a trade-off between the key performance variables, *viz.*, sensitivity and reproducibility versus economy variables, *viz.*, cost and throughput.[6,7] Toward addressing this challenge, we describe the preparation of periodic metal nanoparticle cluster arrays for SERS with fine-tunable cluster sizes and intercluster separations exploiting directed self-assembly using amphiphilic copolymer templates.

Nanoparticle aggregates of noble metals are attractive for SERS sensors due to the strong electromagnetic field enhancements arising at the interparticle junctions upon interaction with visible radiation. Nanoparticle aggregates have been shown in the literature using techniques such as electron-beam lithography (EBL),[8−12] evaporative self-assembly,[13] binding to functionalized surfaces,[14−18] and cluster formation in

* Address correspondence to krishnamoorthys@imre.a-star.edu.sg (S.K.); praveen@prochemsolutions.com (P.T.).

Received for review September 23, 2011 and accepted February 14, 2012.

Published online February 14, 2012
10.1021/nn203661n

solution.[19,20] Since EBL has limitations in mass production, other, more scalable techniques such as template-driven nanoparticle assemblies[21−25] using DNA, surfactants, block copolymers, carbon nanotubes, electrospun fibers, nanoporous membranes, cylindrical micelles, or microorganisms such as bacteria or viruses have been explored. However, most of these cases are aimed at creating isolated clusters rather than arrays of clusters that exhibit a well-defined spatial relationship with respect to each other. Achieving a well-defined spatial relationship between clusters is however important in order to ensure reproducible intercluster electromagnetic interactions as well as cluster densities. Block copolymers are an excellent choice in this direction, as they can produce templates consisting of periodic and high-density features that can be used to guide nanoparticle cluster formation. Earlier instances in the literature that use copolymer templates have shown gold nanoparticle clusters that are embedded within the copolymer matrix formed by guided *in situ* reduction of gold salt within the P4VP domains of PS-*b*-P4VP thin films.[26] While this provides a means to produce metal nanoparticle clusters, they share some key limitations: (a) the surfaces of the nanoparticles are inaccessible; therefore the surface plasmons cannot be utilized for sensing applications; (b) removal of the polymeric matrices would result in (semi)continuous, "fused" structures, therefore leading to the loss in feature shape and separation; (c) achieving independent control over size and separation of the clusters requires extensive molecular engineering of the copolymer block lengths and block ratios and ensuring compatibility of the nanoparticle surface functionality with respect to the polymeric block. Wang *et al*. demonstrated self-assembly of gold nanoparticles driven by electrostatic attachment on phase-inverted poly(styrene-*b*-2-vinylpyridine) nanorings.[27] Even though the authors have shown the capability to attach particles of different sizes, the complex shape of the transformed nanoring templates does not allow adequate control over the nanoparticle numbers that attach per template feature. This limits the rational design of templates to engineer nanoparticle density per feature. Recently, Lee *et al*. showed the use of quaternized poly(4-vinylpyridine) blocks of poly-(styrene-*b*-4-vinylpyridine) copolymer to attach a single gold nanoparticle per poly(4-vinylpyridine) domain and their utility for SERS.[28] Although promising, this approach limits the achievable nanoparticle density to the density of the P4VP domains. In addition, their use of solvent annealing and quarternization steps adds to processing time and the number of experimental variables. During revision of this article, Cho *et al*. reported SERS substrates consisting of silver nanoparticle cluster arrays prepared by plasma treatment on salt-loaded copolymer reverse micelles.[29] The excellent enhancement offered by their silver arrays is limited by an inherent tendency to oxidize, which makes it less attractive to gold from the standpoint of stability and shelf-life. Although Au clusters can also be achieved in principle by the same approach, their SERS capability in the reported configuration is likely to be lesser in comparison.

In our work, we show enhancement factors of $>10^8$, equivalent to what is shown by Cho *et al*. for the identical probe molecule, yet using preformed gold nanoparticles assembled from aqueous solutions. Gold nanoparticle clusters with controlled number of particles per cluster with interparticle separations down to sub-5 nm, intercluster separations down to 10 nm, and high nanoparticle densities of $\sim 7 \times 10^{11}$/in.^{2} are realized in a cost-effective manner. Excellent SERS performance of these cluster arrays attained on both flat chips and in remote-sensing configurations is demonstrated. Besides demonstrating formation of nanoparticle clusters, we perform an in-depth investigation into the geometry of the clusters using simple models, the numbers obtained from which are taken as input for optical simulations by finite difference time domain (FDTD). The simulations bring out the influence due to the cluster size, shape, and separation toward plasmonic properties in relevance to their SERS performance. Advantages pertaining to the low (<10%) inherent and spatial standard deviations of our template features are found to translate as uniform and reproducible SERS performance. Further, the ability toward the formation of metal patterns on an optical fiber faucet enables SERS analysis to be performed in a remote-sensing configuration with tremendous practical implications.

RESULTS AND DISCUSSION

Fabrication of Cluster Arrays. Gold nanoparticle cluster arrays were fabricated by self-assembly of gold nanoparticles guided by nanopatterns of poly(styrene-block-2-vinylpyridine) (PS-*b*-P2VP) reverse micelles on silicon or glass substrates using the steps illustrated in Figure 1. PS-*b*-P2VP reverse micelle arrays were deposited from 0.5% w/w solutions of *m*-xylene, using polymer with a molecular weight of 114 kDa, $f_{PS} \approx 0.5$, and a PDI of 1.1. Thin films were obtained by spin-coating at 5000 rpm spin speed, on silicon or glass chips, to obtain a center-to-center spacing of 91.2 ± 4 nm. The thin films present a two-dimensional quasi-hexagonally periodic array of P2VP domains, covered with a thin PS film.

The P2VP block by virtue of the basicity of its constituent pyridyl units exhibits a net positive charge in aqueous medium at mildly basic to acidic pH values. This is evident from the isoelectric point of 8.3 measured using electrokinetic measurements performed on the PS-*b*-P2VP thin film coated on the Si surface (Figure 2). The films were subsequently incubated in an aqueous solution containing citrate-stabilized gold nanoparticles (pH = 5.8) with a diameter of

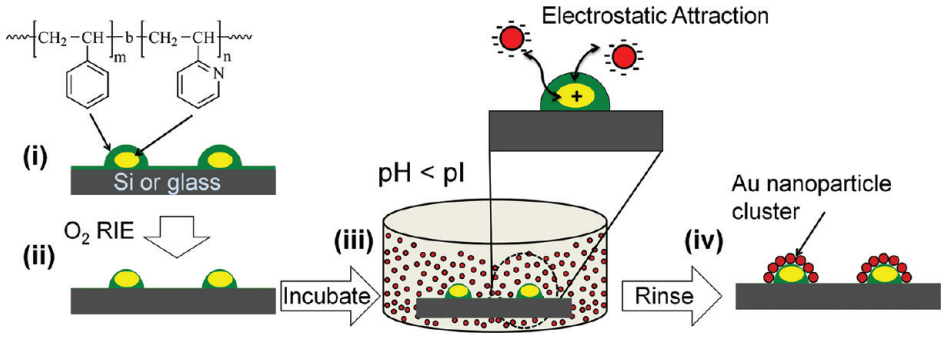

Figure 1. Steps involved in fabrication of gold nanoparticle cluster arrays using polystyrene-block-poly(2-vinylpyridine) (PS-*b*-P2VP) templates on a silicon or glass surface. (i) Spin-coated thin film templates of PS-*b*-P2VP (green indicating a passive outer PS domain, which is neutral, and yellow indicates a positively charged P2VP domain). (ii) Template with reduced feature size obtained upon exposure of the thin films to a controlled oxygen plasma reactive ion etching. (iii) Incubation of the templates in solution of citrate-stabilized colloidal gold nanoparticles at a pH of 5.8. Inset illustrates the electrostatic attraction experienced by the negatively charged gold nanoparticles to positively charged PVP domains within the template. (iv) Gold nanoparticle clusters form around each micellar feature in the template, with the size of the clusters determined by the feature size of the templates.

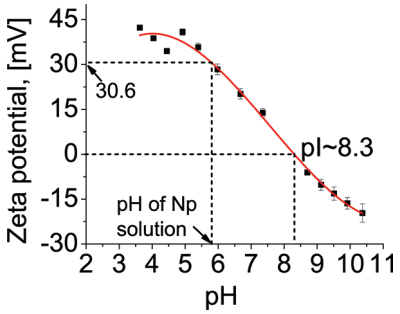

Figure 2. Zeta potential titration of a polystyrene-block-poly(2-vinylpyridine) (PS-*b*-P2VP) thin film performed using electrokinetic measurements on the surface, revealing an isoelectric point of 8.3 and a positive potential of 30.6 mV at pH of 5.8, corresponding to that of the gold nanoparticle (Np) solution.

11.6 ± 0.79 nm (Figure S1 in the Supporting info for diameter histogram). The ζ potential of the nanoparticles was electrophoretically determined to be −38.9 mV. The reverse micelle arrays exhibit a high positive ζ potential value of 30.6 mV at the pH of the nanoparticle suspension. Thus the array of reverse micelles translates into an array of positively charged centers, consequently guiding negatively charged gold nanoparticles by electrostatic attraction. This guides the spatially selective clustering of nanoparticles around each micelle feature. Since the P2VP domains are spatially isolated from each other, the clusters obtained are also spatially well resolved.

Tunability of Geometric Attributes of Nanoparticle Clusters. The geometric attributes of the nanoparticle cluster arrays were thoroughly characterized using plan-view TEM, SEM, and AFM measurements. Since the size of the cluster (defined as the number of particles per cluster, denoted as *N*) is determined by the surface area of the reverse micelle template available for the nanoparticle attachment, tunability in *N* can be achieved by tuning the template dimensions. The template can be tuned by choice of copolymer characteristics, *e.g.*, molecular weight, block composition, or micelle-forming conditions that result in reverse micelles with different aggregation numbers. Alternatively, the template size can also be varied by exposing them to highly controlled oxygen plasma in a reactive ion etcher, to systematically etch the polymer in steps of only a few nanometers. We used the latter route to systematically vary the template size in order to control the number of nanoparticles attached per template feature.

Oxygen plasma RIE exposure with an optimized polymer etch rate of ∼19.2 nm/min resulted in templates with mean heights of 25.8, 21.0, 18.6, and 12.6 nm upon RIE exposure durations of 0 (no RIE exposure), 22, 30, and 38 s (Figure S2 in the Supporting Information for a plot of template height *versus* RIE duration). Incubation of these templates into a gold nanoparticle suspension yielded well-resolved nanoparticle clusters with tunable values of *N*. Nanoparticle clusters of systematically varying sizes, *viz.*, $N \approx 5, 8, 13,$ or 18 nanoparticles/cluster, and low standard deviations are shown in the plan-view TEM images and the histograms in Figures 3 and 4 respectively. The standard deviation observed in the values for *N* follows that of the original templates. The templates exhibit a standard deviation of 11.2% (coefficient of variation in percent) in their as-coated form (*cf.* experimental info for determination of standard deviation). As the size of the templates is reduced using oxygen plasma exposures of 22, 30, and 38 s, the standard deviation increase to 12.6%, 16.5%, and 18.8%, respectively (Figure S3, Supporting Information for size distribution curves). These standard deviations are well within the range that can be reasonably expected for self-assembled systems, *e.g.*, copolymers and colloidal spheres, reported in the literature.[30,31] The templates exhibit a hemispherical cross-section, as evident from the AFM profiles. As a consequence, the resulting nanoparticle clusters exhibit a 3D geometry, as they

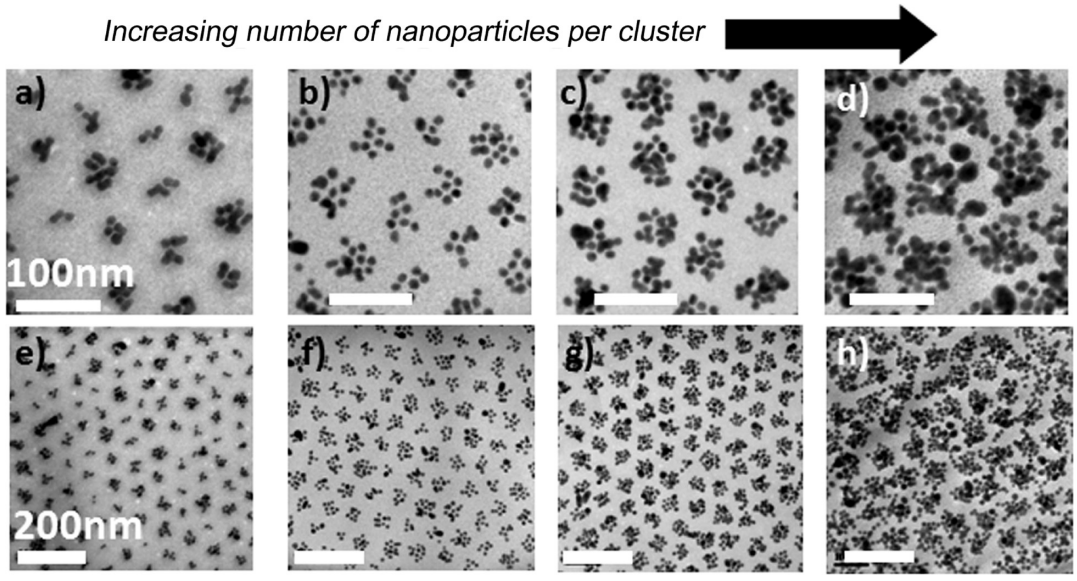

Figure 3. Representative plan-view TEM measurements at (a–d) high and (e–h) low magnifications showing gold nanoparticle clusters with systematically increasing number of particles per cluster. The histograms of the particle numbers per cluster are shown in Figure 4a.

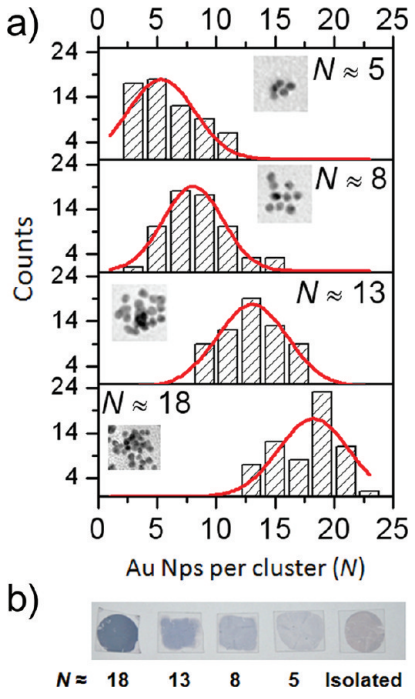

Figure 4. (a) Histograms of the number of particles per cluster for four different template sizes. The average number of particles per cluster (*N*) in each case is indicated. (b) Photographs of glass chips (~1 cm × 1 cm size) consisting of nanoparticle cluster arrays, shown for different values of *N*. The case "isolated" corresponds to unpatterned control, obtained by saturated binding of gold nanoparticles to an aminosilane self-assembled monolayer on glass. The variation in hue with change in cluster size, as well as its uniformity across the coated area of the chip, is discernible.

directly inherit the shape of the templates. The 3D geometry of the clusters can cause artifacts in the plan-view TEM observations, causing the nanoparticles from different planes to sometimes appear fused.

In addition to the tunability in size shown above, tunability in periodicity (center-to-center distance) of the gold nanoparticle clusters can be achieved by fine-tuning the periodicity of the original template features. It is known from literature that the periodicity of the reverse micelle templates can be varied in steps of a few nanometers by varying either the concentration of the reverse micelle solution or the speed of evaporation.[32] In this work, the spin-coating speeds were systematically decreased in the range 5000–1000 rpm to achieve templates with systematically decreasing periodicities from ~92 to ~70 nm. The size of the template features remains constant during this variation, as perceived through their AFM images. Figure 5 shows tapping mode AFM measurements performed on as-prepared templates and the corresponding $N \approx 18$ clusters exhibiting systematic variation of periodicity in steps of only a few nanometers. The AFM measurements show that the cluster formation faithfully followed the nanopatterns defined by the original reverse micelle templates. For the case of nanoparticles with lowest periodicities, the individual clusters in arrays appear less resolved in AFM measurements. This is likely due to AFM tip-convolution effects that prevent effective penetration of the tip between features when feature separations encountered are in the sub-10 nm regime.

Visual inspection of the cluster arrays shows uniformity in hue across the entire coated area, as is perceived from the pictures of coated glass chips shown in Figure 4b. The SEM analysis (Figure S4, Supporting Information) was used to spot any uncovered areas and quantify the yield of the cluster formation. The yield signifies the proportion of the substrate that is covered with nanoparticle clusters with characteristics represented by TEM and AFM measurements shown in Figures 3 and 5, respectively. On the

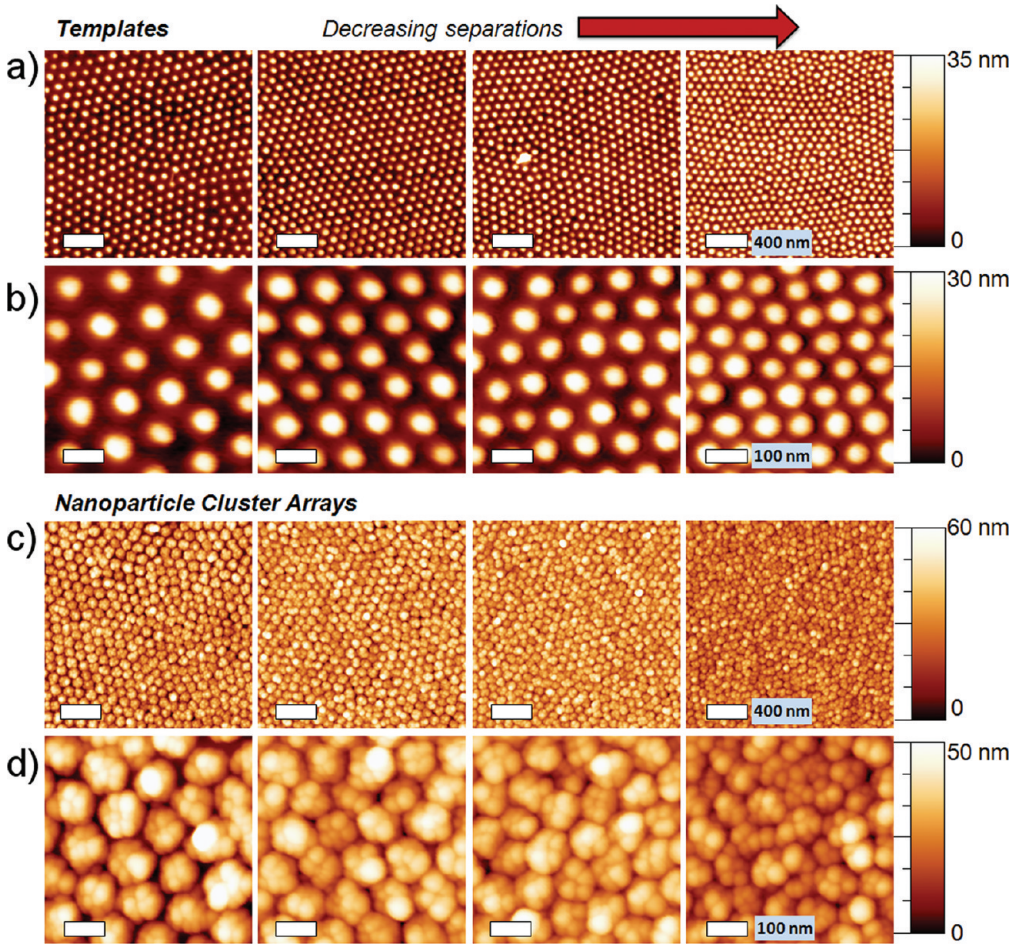

Figure 5. Tapping mode AFM images of the (a, b) templates and (c, d) $N \approx 18$ cluster arrays measured under (a, c) low and (b, d) high resolution, with systematically decreasing separations from left to right. Images within each row have identical measurement areas.

basis of the observation that no uncovered areas could be spotted in FESEM observation at different areas of the substrate, and observed defects were found to be due to spin-coating artifacts at the extreme corners of the substrate, we quantify the yield of cluster formation to be >90%. In an earlier work we have already shown that the reverse micelle templates can be achieved across large areas such as full wafers with a low standard deviation of <10% in feature size and periodicity.[33] In combination with the observation that the cluster formation faithfully occurred at each template feature, the cluster arrays can be expected to inherit the spatial uniformity of the original templates across full wafers. This is an aspect of high importance toward the utility of these arrays for SERS, as the uniformity of the cluster arrays would contribute toward to a low signal intensity variation, and the high-throughput in fabrication would translate into economic means of fabricating the SERS substrates.

Geometric Attributes of Clusters: Modeling Interparticle and Intercluster Separations. Unlike values for size and periodicity of the nanoparticle cluster arrays that are readily determined from TEM and AFM measurements, respectively, the determination of interparticle and intercluster separations is not straightforward. Although the TEM measurements show interparticle separations of <5 nm within the cluster, the nonplanar 3D geometry of the clusters complicates the observation and renders this interpretation deceptive. Knowledge of the interparticle separation within the cluster and intercluster separation within the array is vital as inputs to quantify trends in optical and SERS properties of the cluster arrays and to establish a clearer understanding through simulations. In order to extract these values, we therefore construct imaginary models that accept experimentally determined values for height and density of template features and diameters of gold nanoparticles as input.

$$A_{\text{template}} = 2\pi R^2 \quad \text{(a)}$$

$$A_{\text{Np}} = \pi {r_{\text{eff}}}^2 \quad \text{(b)}$$

$$N = \frac{pA_{\text{template}}}{A_{\text{np}}} = \frac{2p}{{r_{\text{eff}}}^2} R^2 = CR^2, \text{ where } C = \frac{2p}{{r_{\text{eff}}}^2} \quad \text{(c)}$$

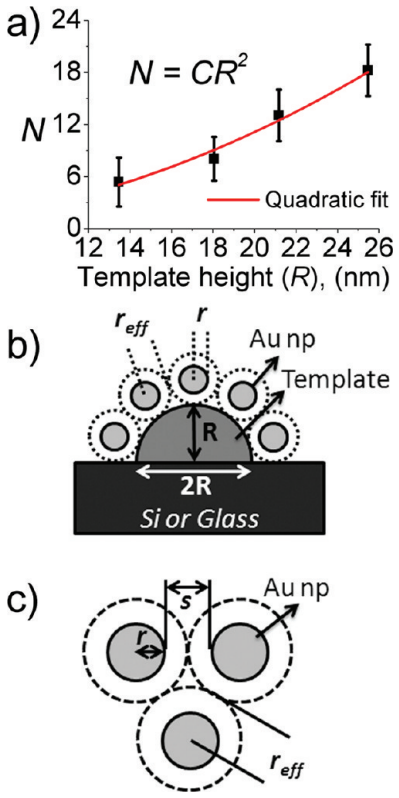

Figure 6. (a) Variation of the number of nanoparticles per cluster (*N*) as a function of height (*R*) of the templates. The quadratic fit of the form $y = Cx^2$ is taken to represent eq c to derive the value for the effective radius r_{eff}. (b) Illustration of the nanoparticle clusters adsorbed on top of the hemispherical polymer template with radius *R*, shown in cross section. (c) Illustration of the triangular lattice assumed for modeling, denoting the actual and effective radii of the nanoparticles (*r* and r_{eff}, respectively) and separation, *s*, caused by the repulsive interaction due to the presence of negatively charged citrate ligands.

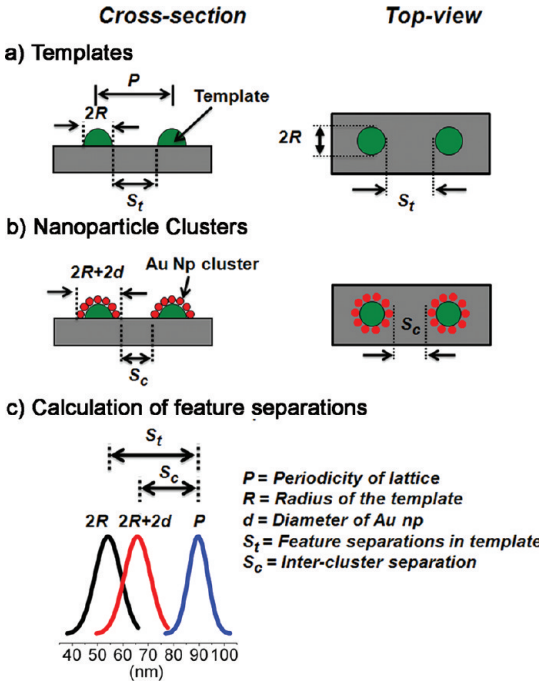

Figure 7. Illustration of the geometric attributes of (a) templates and (b) nanoparticle clusters and the (c) estimation of edge-to-edge separation between the templates and the nanoparticle clusters from experimentally determined distributions in *R*, *d*, and *P*.

$$r_{eff} = \sqrt{\frac{2p}{C}} \quad \text{(d)}$$

$$s = 2(r_{eff} - r) \quad \text{(e)}$$

The calculation of interparticle separations involves calculating the 2D parking space available per nanoparticle on the surface of the template feature (Figure 6 and eqs a–e). The available parking space per particle is obtained by dividing the surface area of the template feature by the footprint of "*N*" nanoparticles. Based on their AFM profile, the templates can be well-approximated as hemispheres (Figure 6b), and thus their surface area is given by eq a. The footprint of each nanoparticle is taken to be a circular area with an "effective radius" (r_{eff}) that is larger than the actual physical radius (*r*) of the nanoparticles (eq b). The effective radius is a result of the interparticle repulsion between the nanoparticles. Assuming that the nanoparticles occupy a triangular lattice, the contribution toward this parking space would come from both the effective size and the unused area at the intersection of the nanoparticles (Figure S5). The area at intersections is known from the packing efficiency for a 2D hexagonal closed packed (hcp) lattice to be 90.6%. The ratio of the surface area of the template to the footprint per nanoparticle provides *N* (eq c). It can be seen that *N* is a quadratic function of *R*. Therefore, by fitting a quadratic function of the form of $y = Cx^2$ to the plot of *N versus R* as shown in Figure 6a, the value of the fitting coefficient (*C*) can be used to deduce r_{eff} using eq d. The interparticle separation (*s*) is twice the difference between the effective and the actual radii of the particles as shown in eq e and in Figure 6c. The goodness of the *N versus R* quadratic fit was confirmed with an adjusted-R^2 value of 0.98. The values of r_{eff} and *s* were thus deduced to be 8.2 and 4.6 nm, respectively. This value for interparticle separation between the particles is indicative of the thickness of the electrical double layer (or Debye length), which depends on the ionic strength of the medium.[18,34]

Although this model assumes for simplicity an equal distance between nanoparticles within the cluster, a distribution in interparticle separations is expected due to the size distribution of the nanoparticles as well as the random nature of adsorption of the nanoparticles on the template features. Such a scenario of irreversible adsorption of monolayers of charged colloids on oppositely charged surfaces has been studied extensively using random sequential adsorption (RSA) models.[35,36] The maximum attainable surface coverage, also known as the "jamming limit",

has been predicted to be 54.7% based on these models.[18,37,38] In our case, the surface coverage of the nanoparticles on the surface of the polymeric templates can be estimated to be ~47%. This represents a fairly high coverage, approaching the jamming limit of RSA. Such coverage attained within a duration of 2 h suggests an enhanced kinetics of adsorption, in contrast to the case of unpatterned polyelectrolyte films investigated in the literature.[39,40] The enhanced kinetics and density could arise from confinement of adsorption within nanopatterns, as has been reported earlier[41−43] for biomolecular adsorption within nanopatterns. Such similarity in behavior to biomolecules may permit use of nanoparticles as a simple model for investigation of biomolecular interactions on patterned surfaces.

Figure 7 illustrates the means of estimating edge-to-edge separations between the clusters using experimentally determined values for feature width and periodicity (average center-to-center distance) of features obtained from AFM and the diameter (*d*) of gold nanoparticles obtained from TEM as input. The periodicity can be calculated from the density of features known from analyzing the AFM images (*cf.* Experimental Section, on image analysis) and by assuming a two-dimensional hexagonal lattice. The separation between the nanoparticle clusters is then estimated by subtracting twice the diameter of the gold nanoparticles from the periodicity of the lattice (Figure S5). The separations obtained in each of the cases shown in Figure 5 could be readily estimated using this model as 61.0, 53.3, 45.5, and 33.7 nm for the templates and 37.6, 29.9, 22.1, and 10.2 nm for the $N \approx 18$ particle clusters, respectively. The estimated values for intercluster separations are in good agreement with what is perceived in the plan-view TEM images (Figure 3), confirming the validity of the model used. The narrow distribution and uniformity of the templates contribute to the ease of modeling to arrive at these numbers for geometric characteristics with fair accuracy. These numbers are necessary as inputs for modeling and simulation of the optical properties of these clusters, as shown later.

Optical Properties of Nanoparticle Cluster Arrays. The optical properties of the cluster arrays were studied using extinction measurements performed using a microspectrometer on areas measuring 77 μm × 77 μm on a chip. A thorough investigation of the size, shape, and interparticle and intercluster separations, along with the respective standard deviations derived from the earlier parts, enables a detailed understanding of the plasmonic properties of the clusters and what could be expected of their SERS performance.

The extinction spectra reveal a single broad peak around ~600 nm, red-shifted by up to ~100 nm in comparison to that of isolated Au nanoparticles (Figure 8). Since each extinction spectrum averages optical properties from numerous clusters, the standard deviation in *N* and interparticle and intercluster separations are

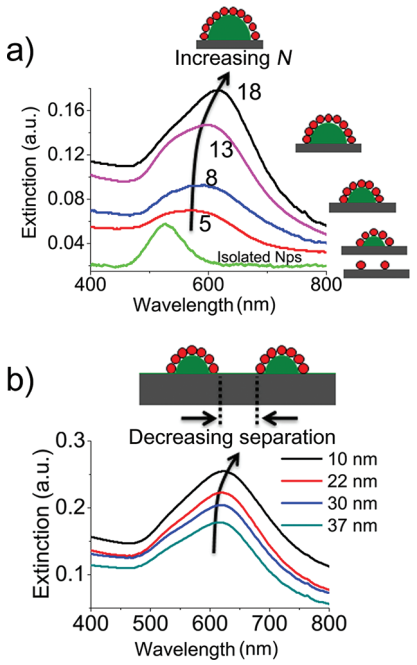

Figure 8. Extinction spectra comparing (a, b) gold nanoparticle cluster arrays with systematically increasing values of *N* and decreasing values of separation. (a) Extinction spectra of nanoparticle clusters show an increase in plasmonic peak intensity and wavelength in the range 590−620 nm with an increase in *N* from 5 to 18. (b) Extinction spectra for $N \approx 18$ clusters show a systematic increase in peak intensity and wavelength with systematic decrease in intercluster separations.

likely to contribute to the broadening of the observed spectral line width.[30] A systematic red-shifting of resonance peak position as well as an increase in the peak intensity is noticed with an increase in cluster size and decrease in intercluster separations. Such red-shifting of the plasmon resonance is known to arise due to strong coupling of localized surface plasmons between adjacent metal nanostructures.[44−46] Plasmonic coupling is known to be a sensitive function of the interparticle separation as well as the number of nearest neighbors.[46,47] In the case of clusters shown here, the average interparticle separation of 4.6 nm (estimated by geometric modeling) is lower than the particle radius of 5.8 nm, based on which an excellent coupling is expected. The strong plasmon coupling is found to manifest itself as a large shift in resonance peak position as a result of cluster formation.

The extinction spectra of the cluster arrays are in sharp contrast to reports for random gold nanoparticle aggregates reported in the literature, where a predominant peak corresponding to the isolated particles appears at ~520 nm with only a broad low-intensity peak corresponding to clusters above 600 nm.[39,48,49] Therefore, the absence of a distinct contribution due to individual Au nanoparticles in our cluster arrays suggests the existence of nanoparticles mainly as clusters. As a consequence, our ordered cluster arrays can be expected to exhibit low variation in interparticle

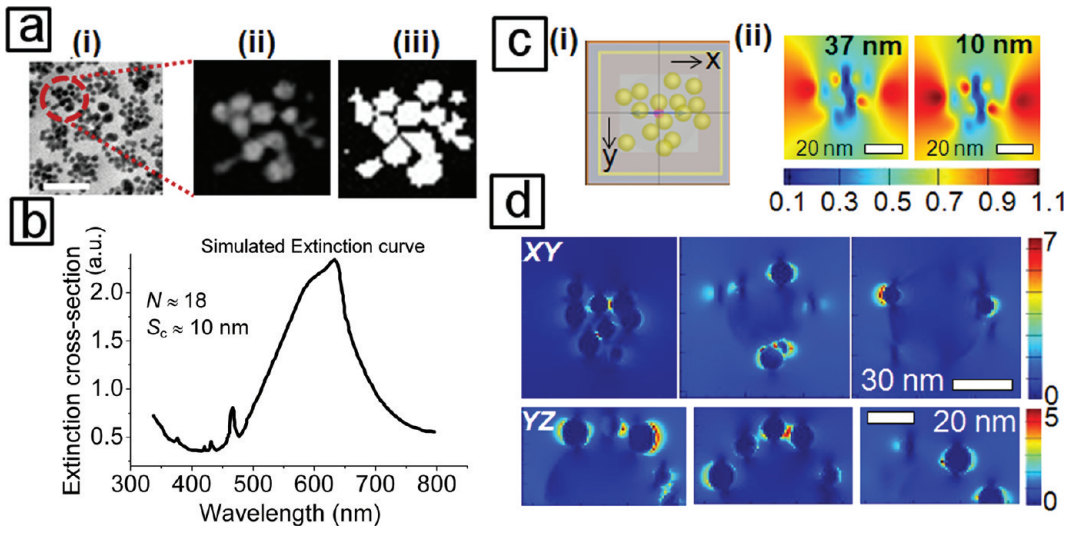

Figure 9. (a) (i–iii) Steps followed to extract coordinates of nanoparticles from TEM plan-view image. (i) TEM plan-view image of $N \approx 18$ clusters from which (ii) one cluster was randomly chosen and (iii) thresholding done to identify the nanoparticle coordinates. (b) Simulated extinction spectrum of $N \approx 18$ clusters shown in (ii) by the FDTD method using unpolarized radiation with an excitation wavelength of 633 nm. (c) (i) Model of the 3D cluster used for FDTD simulations. (ii) False color plots showing the electromagnetic near-field distribution at intercluster separations of 37 and 10 nm, showing an increase in E-field intensity within and around the clusters with a decrease in separation. (d) False color plots showing the electromagnetic near-field distribution of the cluster arrays across *XY* and *YZ* sections shown at 10 nm intervals, revealing hot-spots within the cluster.

separations in comparison to random nanoparticle clusters reported in the literature. The extinction spectra of the cluster arrays reveal certain key aspects of interest for their exploitation in SERS, *viz*., strong plasmonic coupling between nanoparticles and low variation in interparticle separations, which would translate into high density of hot-spots, sought after for highly sensitive SERS detection.

Modeling and Simulation of Optical Properties. Numerical simulations using the FDTD method were performed in order to determine the influence of the cluster size, shape, and interparticle and intercluster separations on the resulting plasmonic properties of the cluster arrays. This is essential to understand the contributing factors to the optical properties of the nanoparticle clusters and to evolve design rules to maximize SERS enhancements. In order to match the experimental system as closely as possible, the model used for the FDTD was developed by extracting (*x, y*) coordinates of nanoparticles belonging to a representative nanoparticle cluster from the TEM plan-view image. The *z* coordinates of the nanoparticles are then calculated from the obtained (*x, y*) coordinates by taking into account the experimentally determined values for template heights and Au NP diameter as input (Figure S5, Supporting Information). Figure 9a illustrates steps to extract (*x, y, z*) coordinates for a randomly chosen cluster corresponding to the $N \approx 18$ cluster arrays. A part of the TEM image representing a well-isolated cluster is sectioned (Figure 9a (ii)), and the center of sectioned image is taken to be the origin. The sectioned image is then subjected to an intensity threshold to obtain the well-resolved location of Au particles, as shown in Figure 9a (iii). The (*x, y*) coordinates of each Au nanoparticle are obtained with respect to the chosen origin, with the distances known through magnification of the TEM image. To extract the *z* coordinates of the nanoparticle, imaginary planes of different *Z* heights are chosen by isolating each individual particle from the threshold image by background subtraction. Then each sectioned nanoparticle template is uploaded into the FDTD simulation layout containing a polystyrene hemisphere on silicon substrate via image import options provided by the FDTD software. The *z* coordinate of the particle is computed from the point of intersection of the Au nanoparticle and the PS sphere. Figure 9c (i) represents the FDTD layout made from the extracted (*x, y, z*) data of each nanoparticle in the sectioned cluster. The simulated layout almost resembles the sectioned Au cluster, except for the particle size, which is assumed to be monodisperse and equivalent to the experimentally determined average size. To double confirm, the *z* coordinates of the Au particle on the polystyrene sphere was also estimated mathematically from the known values for the radius of the PS hemisphere and (*x, y*) coordinates obtained from the plan-view TEM image. The 3D shape of the clusters was thus taken into consideration during this processing.

The interparticle distances computed from the (*x, y, z*) coordinates show an average of 4.2 nm, which agrees well with the value of 4.6 nm predicted by the geometric modeling discussed earlier. The simulated extinction spectrum of $N \approx 18$ clusters shown in Figure 9b was found to closely match the experimental spectrum shown in Figure 8. The simulations were also

similarly carried out for other cluster sizes and were found to match the experimental spectra (Figure S6, Supporting Information for simulated extinction spectra for other cluster sizes). A sharp feature at ~450 nm appearing in the FDTD is found to be absent in the experimental spectrum. This is likely to be due to the inherent assumption of a perfectly periodic lattice in the FDTD simulations that can lead to a grating effect, as observed before[50,51] in the literature. This was further confirmed by repeating the simulations by removing the periodic boundary conditions, which showed the absence of this peak (Figure S7, Supporting Information).

Further, the simulations predict electromagnetic field (E-field) enhancement spanning the entire intercluster space arising due to intercluster plasmonic coupling resulting from the 3D shape of the clusters. Simulations performed on gold nanoparticle clusters with comparable cluster sizes in planar geometry were found to produce no such enhancement (Figure S9, Supporting Information). This has important implications for SERS, as signal enhancements can be expected not only for molecules at the vicinity of hot-spots at nanoparticle junctions but also for those that are present in the intercluster space. This is significant, considering the fact that the intercluster region constitutes 30−60% (depending on the cluster separation, estimated for $N \approx 18$ clusters) of the surface exposed to the laser spot. Further, a decrease in intercluster separation was found to enhance the E-field enhancement both within and around the cluster. Figure 9c shows simulated E-field profiles for intercluster separations of 37 and 10 nm that reveal higher intercluster and interparticle field enhancement at a separation of 10 nm (Figure 9c (ii)). The simulations reveal strong interparticle coupling between nanoparticles within the cluster, making each cluster behave like a "hot-particle". The E-field profiles simulated every 10 nm along the *YZ* and *XZ* directions confirm hot-spots with strong E-field enhancements resulting from such plasmonic coupling within the cluster (Figure 9d). The simulations further point to strong interparticle plasmonic coupling as the likely cause of nonappearance of the peak due to individual Au nanoparticles of ~520 nm in the experimental spectra. This was confirmed by modeling the nanoparticles as half dielectric metal shells, where the interparticle plasmonic coupling is significantly reduced. In such a case the simulated spectrum shows a dominant contribution at ~530 nm accompanied with an absence of peak at ~620 nm (Figure S8, Supporting Information). Thus the dominant contribution at ~620 nm in the experimental extinction spectra of the cluster arrays confirms the presence of strong interparticle plasmonic coupling as well as the existence of nanoparticles mainly within clusters. Well-defined clusters obtained in our experiments are therefore expected to result in a high yield of hot-spots, making them especially attractive for SERS.

SERS Performance on Flat Chips. Uniform nanoparticle cluster arrays shown so far with a high density of junctions between nanoparticles exhibiting separations down to <5 nm are expected to deliver excellent SERS performance. The SERS detection performance of the cluster arrays was investigated using crystal violet (CV) as the model molecule. This was performed by incubating the cluster array substrates for 3 h in 1 μM CV and measuring the SERS spectrum using a laser wavelength of 633 nm and a laser power of 0.63 mW, with an exposure duration of 10 s through a 20× objective lens. The choice of excitation wavelength was made based on its proximity to the peak absorbance of the nanoparticle cluster arrays. There is evidence in the literature that supports the need for tuning the laser wavelength to match the LSPR wavelength of the SERS substrate as a favorable condition to achieve high sensitivity in detection.[52,53] For cluster arrays on both Si and glass substrates, the choice of the 633 nm laser is well justified, as it falls within the plasmonic absorbance spectrum and close to the peak positions. CV has been used for the comparison of SERS results by various other groups in spite of the highly fluctuating nature observed for the SERS spectrum of the molecule.[54] In fact the use of a molecule that is known to exhibit high variation is more suitable to challenge the substrate performance in terms of analysis of point-to-point variation. Incidentally, detection of CV is also used to monitor its illicit use in aquaculture industry[55] as an antimicrobial agent in spite of its toxicity and mutagenicity to mammalian cells.[56]

The SERS performance of the cluster arrays was investigated as a function of varying cluster sizes and intercluster separations. The most intense peak of CV at 1617 cm^{-1} was chosen for comparison of different substrates and to calculate the SERS enhancement factors (EF) (*cf.* Experimental Section for details of the calculation). The signal enhancement by the cluster arrays was compared against unpatterned colloidal monolayers consisting of citrate-stabilized gold nanoparticles adsorbed on amine-terminated self-assembled monolayers of silane on glass or silicon substrates. Figure 10 shows a systematic increase in SERS signal intensities and the enhancement factors with increasing N and decreasing S_c reaching a maximum for $N \approx 18$ clusters at $S_c \approx 10$ nm. The trend in SERS signal intensity with variation in N and S_c was found to match the trend in average nanoparticle densities on the surface. An increase in the number density of nanoparticles can be expected to translate into a high yield of hot-spots for SERS, particularly when the clusters are uniform, as suggested by extinction measurements. The high SERS enhancements exhibited by the cluster arrays are therefore consistent with experimental[57−59] and theoretical[60,61] investigations in the literature, which have shown the dependence of SERS enhancement on the density of hot-spots.

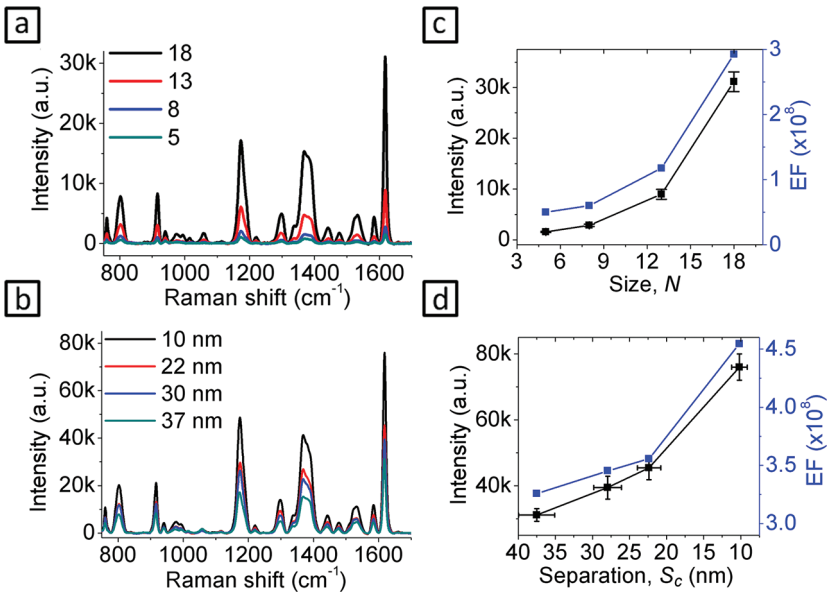

Figure 10. SERS spectra of crystal violet measured on gold nanoparticle cluster arrays show signal intensity enhancement with (a) increasing values of *N* and (b) decreasing values of intercluster separations. (c, d) Plots of the variation in SERS signal intensities corresponding to the most intense peak of CV and the calculated enhancement factors (EF) as a function of (c) cluster size (*N*) and (d) intercluster separations (S_c), respectively.

The uniformity of hot-spots across the sample is confirmed by a low standard deviation of <10% in SERS signal intensities (Figure S10, Supporting Information, for overlaid SERS spectra from 12 different regions on a surface spaced at least 3 mm apart).

A comparison of the cluster arrays with the control samples showed that the controls performed better than the cluster arrays for $N \approx 5$, 8, and 13 clusters. However, the $N \approx 18$ clusters outperformed the control samples for all separations with a maximum enhancement of 272% over that of the controls realized in the case of $S_c \approx 10$ nm (Figure S11, S12 Supporting Information, for comparative plot and spectra). These trends in SERS signal intensities were found to be in tune with the difference in nanoparticle densities achieved on the control samples in comparison to the different cluster arrays. The best performing cluster arrays with $N \approx 18$ at $S_c \approx 10$ nm showed higher density than the controls by ~300%. Besides high nanoparticle densities, an additional contribution to the enhancement by the cluster arrays is expected due to enhanced E-field in the intercluster space arising out of the 3D shape of the clusters, as predicted by FDTD simulations. However, due to the curved nature of the clusters, the E-field is expected to be divergent and as a consequence result in loss due to the scattered photons not falling within the acceptance angle (NA) of the collecting objective (Figure S13, Supporting Information, for schematic illustration). Therefore, making the best out of this contribution may require making adjustments to the experimental setup to enable higher collection efficiency of the optical system during the SERS experiments.

SERS substrates shown here mark a significant improvement in terms of ease and cost of fabrication over literature reports given that the cluster arrays with the best SERS enhancements can be obtained without use of any expensive equipment or clean-room environment. As an additional comparison, we tested the performance of our substrate against the commercial Klarite substrates (Figure S14, Supporting Information). Spectra recorded under identical conditions revealed that the cluster arrays performed far better in terms of signal intensity and spectral resolution. We further performed experiments to test the stability of the nanoparticle cluster arrays. AFM measurements on the cluster arrays after the SERS experiments show their integrity to be preserved. The clusters were further found to be stable even upon exposure to a 2 M solution of NaCl for the tested duration of 12 h (Figure S15, Supporting Information). Such high stability toward high ionic strength aqueous media is especially important for biosensing applications. The clusters were further confirmed to retain their integrity upon exposure to hydrocarbon solvents, allowing the possibility of a wide range of organic analytes to be detected. A deformation of the clusters is however expected upon exposure to solvents that swell PS and P2VP blocks significantly, such as toluene or ethanol, respectively. This may be avoided by cross-linking the PS and P2VP blocks using UV exposure or bifunctional cross-linkers, shown previously in the literature.[62,63] Following the significant increase in SERS intensities observed for the optimized cluster arrays on flat chips, we proceeded to translate the cluster arrays onto an optical fiber faucet to enable SERS capability in remote-sensing configurations.

SERS Performance on Optical Fibers. To prepare nanoparticle cluster arrays on a fiber faucet, the tip of the

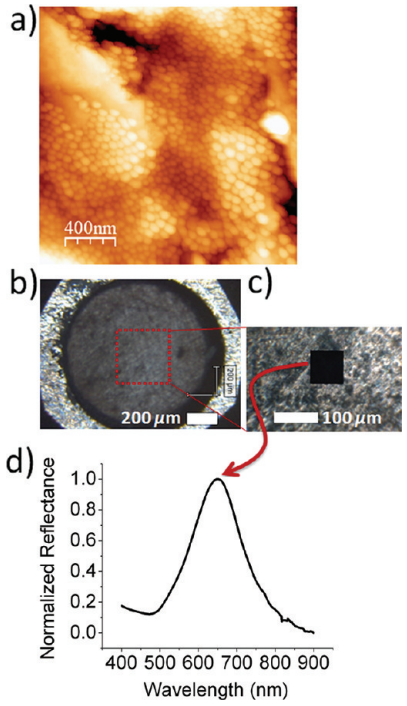

Figure 11. (a) Tapping mode AFM image of the template deposited by drop-coating on the tip of a polished optical fiber. The conformal deposition of the reverse micelles on the rough asperities of the surface of the fiber tip is clearly discernible. (b) Optical picture of the fiber tip covered with gold nanoparticle cluster arrays. (c) The area where reflectance spectra were collected using a spot measuring 77 μm × 77 μm using a microspectrometer. (d) Reflectance spectrum showing plasmonic peak at ~640 nm.

fiber was drop-coated with a solution of PS-*b*-P2VP reverse micelles. In contrast to the case of flat chips where spin-coating speeds was varied to fine-tune the template separations, drop-coating yields a fixed separation that corresponds to the closest 2D packing of the reverse micelles. Such close-packing is evident from the AFM of the templates performed directly on the fiber faucet (Figure 11). In the next step, the fibers coated with the templates were incubated in an aqueous solution of citrate-stabilized gold nanoparticles for 2 h. The conditions used were maintained the same as for the preparation of nanoparticle cluster arrays on flat chips. The resulting nanoparticle arrays were characterized using microspectrometry, which allowed acquiring reflectance measurements on areas measuring only a few tens of micrometers across. The reflectance spectrum was acquired in microscopic spot areas measuring 77 μm × 77 μm that reveal a prominent peak at ~640 nm due to the plasmonic absorbance from the nanoparticle cluster arrays (Figure 11a–c). The uniformity of the nanoparticle cluster arrays could be confirmed by the excellent uniformity in peak-wavelength positions for spectra recorded at different areas of the fiber faucet. The observed peak wavelength of 640 nm in the case of nanoparticle clusters formed on the fiber faucet suggests intercluster separations even lower than the smallest separations we observed on the flat chips. This can be supported by the scenario of close packed template features resulting from drop-coating of the reverse micelles, which in turn would result in closely separated nanoparticle clusters.

The imaging of the nanoparticle cluster arrays formed on the fiber faucet by scanning electron microscopy was complicated by the heavy charging of the nonconducting glass substrate. The AFM measurements on the other hand are significantly limited due to tip-convolution effects for ultralow separations as encountered in this case. Therefore, as evidence for nanoparticle cluster formation on the fiber, we rely on the AFM imaging to confirm formation of templates and optical absorbance to confirm formation of gold nanoparticle clusters, both measurements performed directly on the fiber faucet.

The SERS performance of the optical fiber was tested by using CV as the model analyte as done for the flat chips. The configuration used for measuring the SERS response by the fiber faucet dipped into the CV solution is illustrated in Figure 12a–c. The fiber end consisting of the clusters is dipped into a vial containing the CV solution, while the SERS spectrum is measured through the other end of the fiber, which faces the objective lens of the Raman spectrometer. The remote-sensing measurements clearly reveal both higher signal intensity and lower signal intensity variation among the fibers with clusters as compared to the control fibers (Figure 13). SERS measurements were also performed in the backscattering geometry ("direct" configuration) in order to validate the performance of the cluster arrays formed on the fiber faucet as well as to compare against intensities obtained by remote sensing. The SERS spectra acquired on the fiber faucet in the direct configuration show comparable signal intensities with those observed in the case of cluster arrays with the lowest separations on flat chips ($N \approx 18$, $S_c \approx 10$ nm). This is consistent with what could be expected due to narrow intercluster separations naturally realized on an optical fiber faucet due to the close-packed arrangement of the drop-coated reverse micelles. SERS signal intensity in the remote-sensing configuration was found to be ~10% of that obtained in direct configuration with an estimated EF of 4.7×10^7. A comparison with unpatterned nanoparticle control fibers shows higher SERS intensities for the cluster array containing fibers by ~136% and ~636% for measurements performed in remote-sensing and direct configurations, respectively.

While these experiments demonstrate the promise of the nanoparticle clusters on a fiber faucet for remote sensing, we envisage a significant scope for further improvement in sensitivity, by an appropriate choice of both optical fibers and optical processing employed. Due to combined advantages derived from the self-assembly of colloids and the spatial resolution offered by the

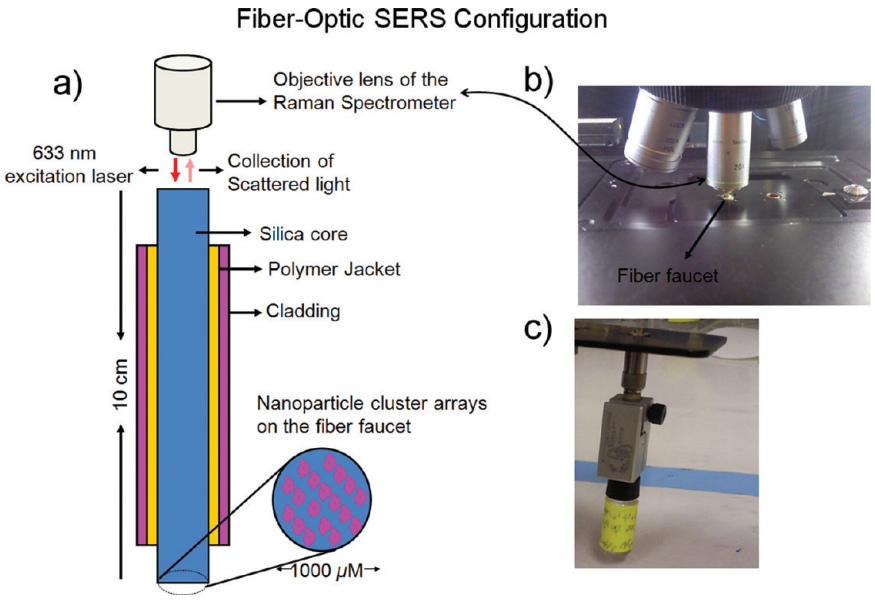

Figure 12. (a) Optrode configuration employed for measuring SERS through an optical fiber. (b, c) measurement setup demonstrating the remote-sensing configuration for measuring the SERS signal of crystal violet through the optical fiber. Views from (b) above and (c) below the optical stage showing the collection end of the fiber facing the objective and the cluster-coated end dipped into the CV solution contained in a vial, which in turn is held in place through a clamp.

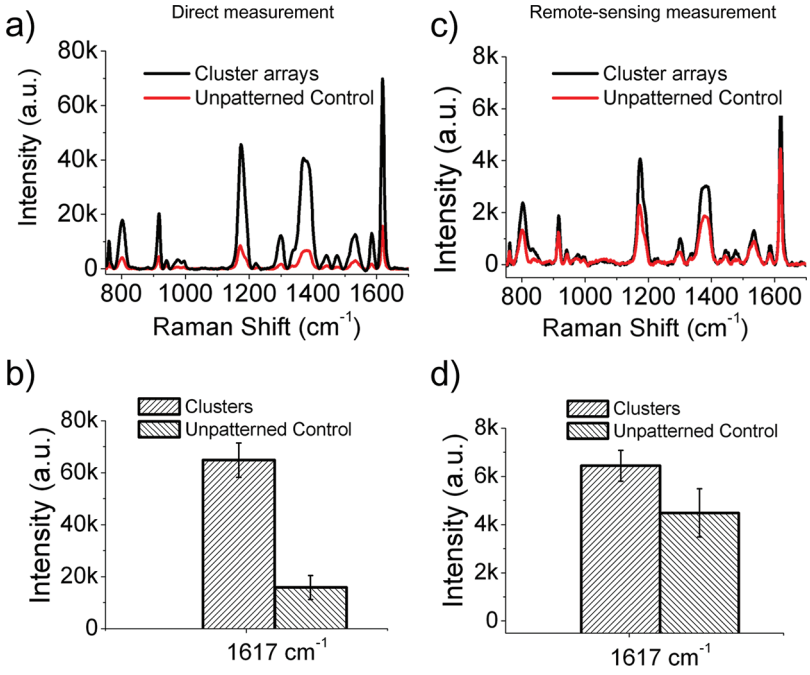

Figure 13. Comparisons of the SERS signal intensity for the most intense peak of the crystal violet molecule, measured under (a) direct and (b) indirect configurations for nanoparticle cluster arrays *versus* unpatterned controls. The unpatterned control consists of isolated nanoparticles obtained by electrostatic adsorption of gold nanoparticles to aminosilane-treated fiber. The direct measurement configuration measures SERS under backscattering geometry on the fiber tip surface incubated in crystal violet solution overnight. The indirect configuration corresponds to SERS measurement performed through the fiber, with the cluster-containing end dipped in solution and the other end facing the objective (as in Figure 12 b,c).

copolymer templates, our approach is attractive over other approaches for fabricating SERS-active optical fibers, *viz.*, random colloid assemblies,[64] surface roughening approaches,[65] or nanostructure transfer approaches[66] reported earlier. The significance of our approach stems from the ease of achieving conformal monolayer coverage of templates on the optical fiber faucet without having to depend on any expensive equipment nor special clean room or environmental conditions. Further, any surface roughness on the fiber faucet seriously limits the capability of most commonly used nanofabrication

approaches in efficiently catering to patterning of optical fiber faucets. In our case, despite the fact that the fiber tip was rough, the conformal template coverage and their facile translation into nanoparticle clusters contribute to their promise in remote-sensing configurations.

CONCLUSIONS

In summary, we have demonstrated simple, yet highly promising means of producing macroscopic arrays of gold nanoparticle clusters with engineered SERS response on both flat and 3D substrates. Au nanoparticle cluster arrays with systematic variation in cluster size and intercluster separations, exhibiting interparticle separations down to sub-5 nm and intercluster separations down to 10 nm, with yields of >90% are demonstrated. Optical modeling and simulations predicted the best electromagnetic enhancements arising out of cluster arrays with the largest size ($N \approx 18$) and smallest separations ($S_c \approx 10$ nm), which correlate well with SERS experiments. The ability to obtain templates conformally on 3D substrates allowed convenient translation of the nanoparticle cluster arrays onto the tip of an optical fiber, enabling SERS measurements in remote-sensing configurations. The benefits of the highly sensitive cluster array configuration observed on flat chips could be carried over to optical fibers as well. We anticipate that the investigations presented here can be further extended along directions of fine-tuning cluster geometry, optimizing the fiber configuration as well as other optical processing parameters. This can pave the way to a reliable and promising SERS detection platform that can efficiently cater to the ever-increasing need for sensitive and remote monitoring of various analytes in biological and chemical environments. The optical properties of these cluster arrays are very promising for applications beyond SERS, in other research areas such as metal-enhanced fluorescence, photocatalysis solar cells, plasmonic waveguides, and light-emitting diodes.

EXPERIMENTAL SECTION

Materials. Polystyrene-block-poly(2-vinylpyridine) (PS-*b*-PVP) (57000-*b*-57000 g/mol) was purchased from Polymer Source Inc. (Montreal, Canada). Silicon and quartz substrates were purchased from Silicon Valley Microelectronics (SVM, CA, USA). (3-Aminopropyl)trimethoxysilane (APTMS, 95%), crystal violet, and sodium citrate dihydrate (~99%) were purchased from Sigma-Aldrich. Toluene (≥99%) was purchased from Merck. Hydrogen tetrachloroaurate(III) trihydrate ($HAuCl_4 \cdot 3H_2O$) (≥99.9%) was purchased from Aldrich. Optical fibers with 1000 μm diameter and 0.37 numerical aperture having a hard polymer cladding with a silica core were purchased from Thorlabs (BFH37-1000, fiber ID F10-056T).

Methods. *Fabrication of Nanoparticle Clusters on Flat Chips.* The silicon and glass substrates were cleaned by ultrasonicating in acetone followed by 2-propanol and finally treated with UV/ozone. A 0.5% (w/w) solution of the polymer was prepared in *m*-xylene. The micelles were deposited onto the substrates by spin-coating at speeds ranging from 1000 to 5000 rpm. The micellar film was subjected to a controlled exposure to oxygen plasma (30 W, 65 mT, 20 sccm) for durations of 20, 35, and 50 s to obtain polyelectrolyte templates of different sizes. Either the as-coated templates or templates with different sizes obtained after oxygen plasma exposure were immersed in a citrate-stabilized gold nanoparticle suspension (pH 5.8) for 2 h followed by rinsing in deionized water. Gold nanoparticles were prepared according to the method reported previously.[49]

Fabrication of Control Substrates. Control substrates with unpatterned gold nanoparticles were prepared by first functionalizing the flat chips or optical fiber faucet with (3-aminopropyl)-trimethoxysilane in vapor phase, followed by their incubation in aqueous solution of citrate-stabilized gold nanoparticles for 12 h. Prior to silanization, the substrates were treated with UV/ozone for 10 min. Silanization was performed within a desiccator under a vacuum of 5×10^{-2} mTorr for 2 h.

Characterization of Cluster Arrays. The zeta potential of the surface coated with micelle arrays was determined by streaming potential measurements using SurPASS electrokinetic analyzer (Anton Par, VA, USA). Electrophoretic measurements on gold nanoparticles were carried out using a Zetasizer Nano ZS (Malvern, Worcestershire, UK), on samples measuring 20 mm × 10 mm. The templates, nanoparticle clusters, and the unpatterned gold nanoparticle controls were characterized with tapping mode AFM (Nanoscope IV Multimode AFM, Veeco Instruments Inc., NY, USA), SEM (FESEM 6700F, JEOL, Tokyo, Japan), and TEM (Philips CM300) operating at 300 kV. The extinction spectra of the gold nanoparticle assemblies on glass substrates were recorded using a CRAIC microspectrophotometer (CRAIC Technologies, CA, USA). An unpolarized light source was used with measurement spot areas of 77 μm × 77 μm.

Image Processing from AFM Data. The AFM images of the templates and the clusters were measured in tapping mode, over areas spanning 2 μm × 2 μm. The standard deviation in the size of the templates was determined from a Gaussian fit made to the height histogram of the templates. The height histograms are more accurate than diameter histograms, as they are not subject to AFM tip-convolution effects. The sigma obtained from the Gaussian fit is divided by the mean to obtain the coefficient of variation. The values for standard deviation reported here represent the coefficient of variance in percent. The feature densities were determined by digitally filtering the image pixels by setting a suitable threshold that isolated the features within the AFM image followed by counting them. The inbuilt "particle analysis" function of the DI Nanoscope software was used for the purpose.

Fabrication of Nanoparticle Clusters on a Fiber Faucet. The fibers were cut into 10 cm pieces by a cleaver. The jacket and cladding were stripped to a length of approximately 1.5 cm from each end. Both ends were then polished using alumina polishing sheets (1 μm) using standard techniques. The polished ends were then washed 2−3 min with a jet of water, sonicated in ethanol for 10 min, and dried. The fiber tip surface was cleaned using UV/ozone treatment. The cladding was protected by wrapping the fiber with aluminum foil, exposing only the tip to plasma.

Optical Simulations. Numerical simulations were performed using the finite-difference time domain method using a commercial software package from Lumerical Solutions, Inc. (Vancouver, Canada). A perfectly matched layer is considered at the top and bottom, and a periodic boundary condition is considered at the sides. The simulations considered a mesh spacing of 1 nm in *x*, *y*, and *z* directions. Unpolarized radiation with an excitation wavelength at 633 nm is employed to excite the sample and is made normally incident through the air medium. The simulations were run by modeling the clusters based on coordinates extracted from TEM images.

SERS Experiments. SERS experiments were carried out using a Raman system (Renishaw InVia, UK) equipped with a microscope, a Peltier cooled CCD detector, and an excitation laser of 633 nm. The system was connected to a microscope (Leica), and the laser light was coupled through an objective lens of 20× (for flat chips) and 50× (for fibers), which was used for exciting the sample as well as collecting the Raman signals. Instrument control and data acquisition were carried out using the WIRE 3.0 software package provided with the Renishaw system. Prior to each Raman experiment calibration of the instrument was done with the Raman signal from a silicon standard centered at 520 cm^{-1}. Subtraction of the baseline using cubic spline interpolation was performed in order to eliminate unwanted background noise and to facilitate data analysis. SERS substrates were incubated for 3 h in 1 μM CV solution. Substrates were taken out and fixed onto the glass slide with a coverslip placed on top. SERS measurements were taken from at least eight random locations that are more than 3 mm apart in the wavenumber range of 400−2000 cm^{-1} with an exposure time of 10 s using 0.63 mW of laser power. For optics fibers, the incubation with 1 μM CV was carried out by dipping the substrate end of the fiber in a vial through a septa. For direct end measurements 0.63 mW laser power is used, whereas for through-fiber measurements 6.3 mW laser power is used. The recorded spectrum after baseline correction using WIRE 3.0 software was imported into OriginPro and processed further for intensity comparisons. SERS enhancement factors (EF, denoted as *G*) were calculated by normalizing the SERS intensities observed on clusters with that obtained on bare Au substrate under identical experimental conditions using the following equation. The packing density of molecules and incorporation of surface roughness factor *R* was followed from literature.[67,68]

$$G = \frac{\frac{I_{SERS}}{N_{SERS}}}{\frac{I_{Raman}}{N_{Bulk}}} = \left(\frac{H\rho}{R\mu}\right)\left(\frac{I_{SERS}}{I_{Raman}}\right)$$

I_{SERS} and I_{Raman} denote Raman spectral intensities for crystal violet at 1617cm^{-1}, recorded on the SERS substrate and in the absence of enhancement, respectively. $N_{Bulk} = AH\rho$ is the number of CV molecules in bulk solution contributing to the unenhanced Raman signal; $N_{SERS} = AR\mu$ is the number of CV molecules on the substrate and contributes to the SERS signal; *A* is the area of the laser spot; *R* is the surface roughness ratio; μ is the packing density of CV molecules on the substrate; ρ is the number of molecules in the CV solution; *H* is the apparent height of the CV liquid layer that emits a Raman signal; *G* is the enhancement factor.

Conflict of Interest: The authors declare no competing financial interest.

Acknowledgment. Funding support received from Joint Council Office (JCO) of the Agency for Science Technology and Research (A*STAR), *via* grant 10/3/EG/05/04, is gratefully acknowledged. The authors are grateful to A. Mlayah (CNRS, France) for helpful discussions, M. Olivo (SBIC, Singapore) and H. Y. Low (IMRE, Singapore) for their kind project support, R. K. Gupta (NTU, Singapore) for help with electrokinetic measurements, Man Hua (SBS, NTU) for technical assistance during SERS experiments, S. Dinda (SOA, Bhubaneshwar) for testing stability of the arrays, H. R. Tan (IMRE) for help with TEM cross-section measurements, and SnFPC IMRE for fabrication and characterization facilities.

Supporting Information Available: Additional information pertaining to fabrication, characterization, optical simulations, and SERS analysis of the nanoparticle cluster arrays is available free of charge *via* the Internet at http://pubs.acs.org.

REFERENCES AND NOTES

1. Hering, K.; Cialla, D.; Ackermann, K.; Dörfer, T.; Möller, R.; Schneidewind, H.; Mattheis, R.; Fritzsche, W.; Rösch, P.; Popp, J. SERS: A Versatile Tool in Chemical and Biochemical Diagnostics. *Anal. Bioanal. Chem.* **2008**, *390*, 113–124.
2. Campion, A.; Kambhampati, P. Surface-Enhanced Raman Scattering. *Chem. Soc. Rev.* **1998**, *27*, 241–250.
3. Luo, B. S.; Lin, M. A Portable Raman System for the Identification of Foodborne Pathogenic Bacteria. *J. Rapid Methods Autom. Microbiol.* **2008**, *16*, 238–255.
4. Jarvis, R. M.; Goodacre, R. Discrimination of Bacteria Using Surface-Enhanced Raman Spectroscopy. *Anal. Chem.* **2004**, *76*, 40–47.
5. Grow, A. E.; Wood, L. L.; Claycomb, J. L.; Thompson, P. A. New Biochip Technology for Label-Free Detection of Pathogens and Their Toxins. *J. Microbiol. Methods* **2003**, *53*, 221–233.
6. Lin, X. M.; Cui, Y.; Xu, Y. H.; Ren, B.; Tian, Z. Q. Surface-Enhanced Raman Spectroscopy: Substrate-Related Issues. *Anal. Bioanal. Chem.* **2009**, *394*, 1729–1745.
7. Tripp, R. A.; Dluhy, R. A.; Zhao, Y. Novel Nanostructures for SERS Biosensing. *Nano Today* **2008**, *3*, 31–37.
8. Talley, C. E.; Jackson, J. B.; Oubre, C.; Grady, N. K.; Hollars, C. W.; Lane, S. M.; Huser, T. R.; Nordlander, P.; Halas, N. J. Surface-Enhanced Raman Scattering From Individual Au Nanoparticles and Nanoparticle Dimer Substrates. *Nano Lett.* **2005**, *5*, 1569–1574.
9. Nordlander, P.; Oubre, C.; Prodan, E.; Li, K.; Stockman, M. I. Plasmon Hybridization in Nanoparticle Dimers. *Nano Lett.* **2004**, *4*, 899–903.
10. Brandl, D. W.; Mirin, N. A.; Nordlander, P. Plasmon Modes of Nanosphere Trimers and Quadrumers. *J. Phys. Chem. B* **2006**, *110*, 12302–12310.
11. Lassiter, J. B.; Sobhani, H.; Fan, J. A.; Kundu, J.; Capasso, F.; Nordlander, P.; Halas, N. J. Fano Resonances in Plasmonic Nanoclusters: Geometrical and Chemical Tunability. *Nano Lett.* **2010**, *10*, 3184–3189.
12. Hentschel, M.; Saliba, M.; Vogelgesang, R.; Giessen, H.; Alivisatos, A. P.; Liu, N. Transition From Isolated to Collective Modes in Plasmonic Oligomers. *Nano Lett.* **2010**, *10*, 2721–2726.
13. Yin, Y.; Lu, Y.; Gates, B.; Xia, Y. Template-Assisted Self-Assembly: A Practical Route to Complex Aggregates of Monodispersed Colloids With Well-Defined Sizes, Shapes, and Structures. *J. Am. Chem. Soc.* **2001**, *123*, 8718–8729.
14. Schmitt, J.; Mächtle, D.; Eck, D.; Möhwald, H.; Helm, C. A. Preparation and Optical Properties of Colloidal Gold Monolayers. *Langmuir* **1999**, *15*, 3256–3266.
15. Kim, K.; Ryoo, H.; Shin, K. S. Adsorption and Aggregation Characteristics of Silver Nanoparticles onto a Poly(4-vinylpyridine) Film: A Comparison with Gold Nanoparticles. *Langmuir* **2010**, *26*, 10827–10832.
16. Malynych, S.; Luzinov, I.; Chumanov, G. Poly(vinyl pyridine) As a Universal Surface Modifier for Immobilization of Nanoparticles. *J. Phys. Chem. B* **2002**, *106*, 1280–1285.
17. Gupta, S.; Agrawal, M.; Conrad, M.; Hutter, N. A.; Olk, P.; Simon, F.; Eng, L. M.; Stamm, M.; Jordan, R. Poly(2-(Dimethylamino) Ethyl Methacrylate) Brushes with Incorporated Nanoparticles As a SERS Active Sensing Layer. *Adv. Funct. Mater.* **2010**, *20*, 1756–1761.
18. Kooij, E. S.; Martijn Brouwer, E. A.; Wormeester, H.; Poelsema, B. Ionic Strength Mediated Self-Organization of Gold Nanocrystals: An AFM Study. *Langmuir* **2002**, *18*, 7677–7682.
19. Qiu, P.; Jensen, C.; Charity, N.; Towner, R.; Mao, C. Oil Phase Evaporation-Induced Self-Assembly of Hydrophobic Nanoparticles into Spherical Clusters with Controlled Surface Chemistry in an Oil-in-Water Dispersion and Comparison of Behaviors of Individual and Clustered Iron Oxide Nanoparticles. *J. Am. Chem. Soc.* **2010**, 567–571.
20. Wark, A. W.; Stokes, R. J.; Darby, S. B.; Smith, W. E.; Graham, D. Dynamic Imaging Analysis of SERS-Active Nanoparticle Clusters in Suspension. *J. Phys. Chem. C 114*, 18115−18120.
21. Grzelczak, M.; Vermant, J.; Furst, E. M.; Liz-Marzán, L. M. Directed Self-Assembly of Nanoparticles. *ACS Nano* **2010**, *4*, 3591–3605.
22. Haryono, A.; Binder, W. H. Controlled Arrangement of Nanoparticle Arrays in Block-Copolymer Domains. *Small* **2006**, *2*, 600–611.
23. Zhang, C. L.; Lv, K. P.; Cong, H. P.; Yu, S. H. Controlled Assemblies of Gold Nanorods in PVA Nanofiber Matrix As Flexible Free-Standing SERS Substrates by Electrospinning. *Small* **2011**.

24. Ko, H.; Singamaneni, S.; Tsukruk, V. V. Nanostructured Surfaces and Assemblies As SERS Media. *Small* **2008**, *4*, 1576–1599.
25. He, D.; Hu, B.; Yao, Q. F.; Wang, K.; Yu, S. H. Large-Scale Synthesis of Flexible Free-Standing SERS Substrates with High Sensitivity: Electrospun PVA Nanofibers Embedded with Controlled Alignment of Silver Nanoparticles. *ACS Nano* **2009**, *3*, 3993–4002.
26. Forster, S.; Antonietti, M. Amphiphilic Block Copolymers in Structure Controlled Nanomaterial Hybrids. *Adv. Mater.* **1998**, *10*, 195–217.
27. Wang, L.; Montagne, F.; Hoffmann, P.; Heinzelmann, H.; Pugin, R. Hierarchical Positioning of Gold Nanoparticles into Periodic Arrays Using Block Copolymer Nanoring Templates. *J. Colloid Interface Sci.* **2011**, *356*, 496–504.
28. Lee, W.; Lee, S. Y.; Briber, R. M.; Rabin, O. Self-Assembled SERS Substrates with Tunable Surface Plasmon Resonances. *Adv. Funct. Mater.* **2011**, *21*, 3424.
29. Cho, W. J.; Kim, Y.; Kim, J. K. Ultrahigh Density Array of Silver Nanoclusters for SERS Substrate With High Sensitivity and Excellent Reproducibility. *ACS Nano* **2012**, *6*, 249–255.
30. Haynes, C. L.; Van Duyne, R. P. Nanosphere Lithography: a Versatile Nanofabrication Tool for Studies of Size-Dependent Nanoparticle Optics. *J. Phys. Chem. B* **2001**, *105*, 5599–5611.
31. Guarini, K. W.; Black, C. T.; Yeuing, S. H. I. Optimization of Diblock Copolymer Thin Film Self Assembly. *Adv. Mater.* **2002**, *14*, 1290–1294.
32. Krishnamoorthy, S.; Pugin, R.; Brugger, J.; Heinzelmann, H.; Hinderling, C. Tuning the Dimensions and Periodicities of Nanostructures Starting from the Same Polystyrene-Block-Poly(2-Vinylpyridine) Diblock Copolymer. *Adv. Funct. Mater.* **2006**, *16*, 1469–1475.
33. Krishnamoorthy, S.; Manipaddy, K. K.; Yap, F. L. Wafer-Level Self-Organized Copolymer Templates for Nanolithography with Sub-50 nm Feature and Spatial Resolutions. *Adv. Funct. Mater.* **2011**, *21*, 1102–1112.
34. Israelachvili, J. N. *Intermolecular and Surface Forces*; Academic Press: London, 1991.
35. Adamczyk, Z.; Zembala, M.; Siwek, B.; Warszyński, P. Structure and Ordering in Localized Adsorption of Particles. *J. Colloid Interface Sci.* **1990**, *140*, 123–137.
36. Adamczyk, Z.; Nattich, M.; Barbasz, J. Deposition of Colloid Particles at Heterogeneous and Patterned Surfaces. *Adv. Colloid Interface Sci.* **2009**, *147–148*, 2–17.
37. Oberholzer, M. R.; Stankovich, J. M.; Carnie, S. L.; Chan, D. Y. C.; Lenhoff, A. M. 2-D and 3-D Interactions in Random Sequential Adsorption of Charged Particles. *J. Colloid Interface Sci.* **1997**, *194*, 138–153.
38. Semmler, M.; Mann, E. K.; Rička, J.; Borkovec, M. Diffusional Deposition of Charged Latex Particles on Water–Solid Interfaces at Low Ionic Strength. *Langmuir* **1998**, *14*, 5127–5132.
39. Schmitt, J.; Mächtle, P.; Eck, D.; Möhwald, H.; Helm, C. A. Preparation and Optical Properties of Colloidal Gold Monolayers. *Langmuir* **1999**, *15*, 3256–3266.
40. Grabar, K. C.; Smith, P. C.; Musick, M. D.; Davis, J. A.; Walter, D. G.; Jackson, M. A.; Guthrie, A. P.; Natan, M. J. Kinetic Control of Interparticle Spacing in Au Colloid-Based Surfaces: Rational Nanometer-Scale Architecture. *J. Am. Chem. Soc.* **1996**, *118*, 1148–1153.
41. Krishnamoorthy, S.; Himmelhaus, M. Confinement-Induced Enhancement of Antigen-Antibody Interactions within Binary Nanopatterns to Achieve Higher Efficiency of on-Chip Immunosensors. *Adv. Mater.* **2008**, *20*, 2782–2788.
42. Agheli, H.; Malmström, J.; Larsson, E. M.; Textor, M.; Sutherland, D. S. Large Area Protein Nanopatterning for Biological Applications. *Nano Lett.* **2006**, *6*, 1165–1171.
43. Valsesia, A.; Colpo, P.; Mannelli, I.; Mornet, S.; Bretagnol, F.; Ceccone, G.; Rossi, F. Use of Nanopatterned Surfaces to Enhance Immunoreaction Efficiency. *Anal. Chem.* **2008**, *80*, 1418–1424.
44. Su, K. H.; Wei, Q. H.; Zhang, X.; Mock, J. J.; Smith, D. R.; Schultz, S. Interparticle Coupling Effects on Plasmon Resonances of Nanogold Particles. *Nano Lett.* **2003**, *3*, 1087–1090.
45. Atay, T.; Song, J. H.; Nurmikko, A. V. Strongly Interacting Plasmon Nanoparticle Pairs: From Dipole- Dipole Interaction to Conductively Coupled Regime. *Nano Lett.* **2004**, *4*, 1627–1631.
46. Jain, P. K.; Huang, W.; El-Sayed, M. A. On the Universal Scaling Behavior of the Distance Decay of Plasmon Coupling in Metal Nanoparticle Pairs: A Plasmon Ruler Equation. *Nano Lett.* **2007**, *7*, 2080–2088.
47. Fan, J. A.; Wu, C.; Bao, K.; Bao, J.; Bardhan, R.; Halas, N. J.; Manoharan, V. N.; Nordlander, P.; Shvets, G.; Capasso, F. Self-Assembled Plasmonic Nanoparticle Clusters. *Science* **2010**, *328*, 1135–1138.
48. Quinten, M.; Kreibig, U. Optical Properties of Aggregates of Small Metal Particles. *Surf. Sci.* **1986**, *172*, 557–577.
49. Grabar, K. C.; Griffith Freeman, R.; Hommer, M. B.; Natan, M. J. Preparation and Characterization of Au Colloid Monolayers. *Anal. Chem.* **1995**, *67*, 735–743.
50. Tan, R. Z.; Agarwal, A.; Balasubramanian, N.; Kwong, D. L.; Jiang, Y.; Widjaja, E.; Garland, M. 3D Arrays of SERS Substrate for Ultrasensitive Molecular Detection. *Sens. Actuators, A* **2007**, *139*, 36–41.
51. Yang, L.; Yan, B.; Premasiri, W. R.; Ziegler, L. D.; Negro, L. D.; Reinhard, B. M. Engineering Nanoparticle Cluster Arrays for Bacterial Biosensing: The Role of the Building Block in Multiscale SERS Substrates. *Adv. Funct. Mater.* **2010**, *20*, 2619–2628.
52. Natan, M. J. Concluding Remarks Surface Enhanced Raman Scattering. *Faraday Discuss.* **2006**, *132*, 321–328.
53. Willets, K. A.; Van Duyne, R. P. Localized Surface Plasmon Resonance Spectroscopy and Sensing. *Annu. Rev. Phys. Chem.* **2007**, *58*, 267–297.
54. Kudelski, A. Raman Studies of Rhodamine 6G and Crystal Violet Sub-Monolayers on Electrochemically Roughened Silver Substrates: Do Dye Molecules Adsorb Preferentially on Highly SERS-Active Sites? *Chem. Phys. Lett.* **2005**, *414*, 271–275.
55. Alderman, D. J. In Vitro Testing of Fisheries Chemotherapeutants. *J. Fish Dis.* **1982**, *5*, 113–123.
56. Srivastava, S.; Sinha, R.; Roy, D. Toxicological Effects of Malachite Green. *Aquat. Toxicol.* **2004**, *66*, 319–329.
57. Wustholz, K. L.; Henry, A. I.; McMahon, J. M.; Freeman, R. G.; Valley, N.; Piotti, M. E.; Natan, M. J.; Schatz, G. C.; Duyne, R. P. V. Structure–Activity Relationships in Gold Nanoparticle Dimers and Trimers for Surface-Enhanced Raman Spectroscopy. *J. Am. Chem. Soc.* **2010**, 10903–10910.
58. Jiang, J.; Bosnick, K.; Maillard, M.; Brus, L. Single Molecule Raman Spectroscopy at the Junctions of Large Ag Nanocrystals. *J. Phys. Chem. B* **2003**, *107*, 9964–9972.
59. Michaels, A. M.; Jiang, J.; Brus, L. Ag Nanocrystal Junctions As the Site for Surface-Enhanced Raman Scattering of Single Rhodamine 6G Molecules. *J. Phys. Chem. B* **2000**, *104*, 11965–11971.
60. Xu, H.; Aizpurua, J.; Käll, M.; Apell, P. Electromagnetic Contributions to Single-Molecule Sensitivity in Surface-Enhanced Raman Scattering. *Phys. Rev. E* **2000**, *62*, 4318–4324.
61. Hao, E.; Schatz, G. C. Electromagnetic Fields Around Silver Nanoparticles and Dimers. *J. Chem. Phys.* **2004**, *120*, 357.
62. Zhang, R.; Cherdhirankorn, T.; Graf, K.; Koynov, K.; Berger, R. Swelling of Cross-Linked Polystyrene Beads in Toluene. *Microelectron. Eng.* **2008**, *85*, 1261–1264.
63. Hayward, R. C.; Chmelka, B. F.; Kramer, E. J. Crosslinked Poly(styrene)-block-Poly(2-vinylpyridine) Thin Films as Swellable Templates for Mesostructured Silica and Titania. *Adv. Mater.* **2005**, *17*, 2591–2595.
64. Stokes, D. L.; Vo-Dinh, T. Development of an Integrated Single-Fiber SERS Sensor. *Sens. Actuators, B* **2000**, *69*, 28–36.
65. Viets, C.; Hill, W. Comparison of Fibre-Optic SERS Sensors With Differently Prepared Tips. *Sens. Actuators, B* **1998**, *51*, 92–99.
66. Smythe, E. J.; Dickey, M. D.; Bao, J.; Whitesides, G. M.; Capasso, F. Optical Antenna Arrays on a Fiber Facet for *in Situ* Surface-Enhanced Raman Scattering Detection. *Nano Lett.* **2009**, *9*, 1132–1138.
67. Wang, Y.; Becker, M.; Wang, L.; Liu, J.; Scholz, R.; Peng, J.; Go sele, U.; Christiansen, S.; Kim, D. H.; Steinhart, M. Nanostructured Gold Films for SERS by Block Copolymer-Templated Galvanic Displacement Reactions. *Nano Lett.* **2009**, *9*, 2384–2389.
68. Cai, W. B.; Ren, B.; Li, X. Q.; She, C. X.; Liu, F. M.; Cai, X. W.; Tian, Z. Q. Investigation of Surface-Enhanced Raman Scattering From Platinum Electrodes Using a Confocal Raman Microscope: Dependence of Surface Roughening Pretreatment. *Surf. Sci.* **1998**, *406*, 9–22.